Highly-accessible, doped TiO$_2$ nanoparticles embedded at the surface of SiO$_2$ as photocatalysts for the degradation of pollutants under visible and UV radiation

Damiano Cani [a], Jan C. van der Waal [b], Paolo P. Pescarmona [c],*

[a] *Centre for Surface Chemistry and Catalysis, KU Leuven, Celestijnenlaan 200F, 3001, Heverlee, Belgium*
[b] *Department of Sustainable Process and Energy Systems, TNO, Leeghwaterstraat 44, 2628 CA, Delft, the Netherlands*
[c] *Chemical Engineering Group, Engineering and Technology Institute Groningen (ENTEG), University of Groningen, Nijenborgh 4, 9747 AG, Groningen, the Netherlands*

ARTICLE INFO

ABSTRACT

A series of photocatalysts consisting of C- and N-doped titanium dioxide (TiO$_2$) nanoparticles highly dispersed and firmly embedded at the surface of a silica matrix were prepared using a novel synthesis method in which activated carbon has a double role: it acts as support for depositing the TiO$_2$ nanoparticles and as hard template for generating a silica matrix that embeds them. Additionally, the use of activated carbon in combination with ammonia during the synthesis led to carbon and nitrogen doping of the TiO$_2$ domains, which enhanced their absorption of radiation in the visible range. The combination of these features led to higher activity (*i.e.* higher removal % and TON) in the photocatalytic degradation of probe pollutants (phenol and rhodamine B) compared to the benchmark P25 TiO$_2$ under UV and, even more markedly, under visible radiation. Particularly, the photocatalyst prepared with 10 wt% of TiO$_2$ nanoparticles (10%TiO$_2$NP@SiO$_2$) displayed much enhanced TON values under visible radiation compared to P25 TiO$_2$ (a 12 times higher TON with rhodamine B, and an 8 times higher TON with phenol). The TON values are also significantly higher compared to any previously reported TiO$_2$-SiO$_2$ photocatalyst. The TiO$_2$NP@SiO$_2$ photocatalysts can be effectively reused in consecutive runs. The photocatalytic activity of the prepared materials was correlated to their physicochemical properties by means of a thorough characterisation using a combination of techniques (XRD, ICP-OES, N$_2$ physisorption, TEM, UV–vis, FT-IR and XPS).

1. Introduction

The development of efficient and cost-effective technologies for the purification of water streams polluted by industry and other human activities is a relevant research target both from the economic and societal point of view. Conventional technologies for water purification include filtration, biological treatments and sedimentation. Since the discovery of the photocatalytic properties of titanium dioxide by Fujishima and Honda in 1972 [1], the exploitation of photocatalysis for the degradation of toxic compounds in water has been extensively studied [2–4]. The main advantages of photocatalysis over commonly used technologies are the possibility of completely degrading organic pollutants into harmless molecules (*i.e.* CO$_2$ and H$_2$O) and to exploit solar radiation as energy source to achieve degradation [5]. Typical heterogeneous photocatalysts are semiconductors that, upon excitation

by absorption of radiation having higher energy compared to their band gap energy [6,7], generate electron-hole couples that can react with O$_2$ and H$_2$O forming radical species such as the superoxide O$_2^{-\bullet}$ and the hydroxyl radical OH$^\bullet$, which can degrade pollutants located at the surface of the photocatalyst or in its proximity [8]. Alternatively, the adsorbed organic molecules can undergo degradation by direct interaction with the electron-hole couples [9]. TiO$_2$ is the most widely employed heterogeneous photocatalyst due to several favourable properties: it has high photocatalytic activity under UV radiation, is highly stable under the operating conditions, is inexpensive and non-toxic [10–12]. However, TiO$_2$ also has clear limitations. The first is related to its band gap energy (3.0–3.2 eV, depending on the relative amount of its two main polymorphs, rutile and anatase), which implies that UV radiation is required for exciting electrons to the conduction band [13], whereas an ideal photocatalyst should be able to absorb visible light (to

maximise the exploitation of solar radiation) to form electron-hole couples that are energetic enough to lead to the desired reaction [14]. Another drawback of TiO_2 is the relatively low specific surface area that characterises bulk transition metal oxides, which is detrimental because the photocatalytic degradation of pollutants involves the adsorption of the reactants (*i.e.* organic pollutants, water and oxygen) on the surface of the photocatalyst. An established approach to increase the specific surface area of titanium dioxide is to prepare it in the form of nanoparticles, as in the case of the benchmark photocatalyst P25 TiO_2 [15–18]. However, nanoparticles have downsides owing to their tendency to agglomerate during the reaction and to the difficulty in separating and fully recovering them from the reaction mixture due to their small size [19]. A strategy that has been developed to overcome these limitations consists in supporting the TiO_2 (or other active phases) on a high surface area material, which can also favour the adsorption of pollutants [20, 21]. In this context, embedding the photocatalytic species in mesoporous silica materials (*e.g.* MCM-41 and SBA-15) through the use of structure directing agents proved to be a successful approach to produce easily reusable and highly active photocatalysts [22–29]. However, these systems are not devoid of issues: (i) high TiO_2 loadings lead to loss of the desired porous structure and (ii) the TiO_2 domains are partially located within the silica walls of the porous framework, and in such case are not accessible for the photocatalytic reaction. In this work, we introduce an original yet straightforward and inexpensive synthetic strategy to tackle these limitations by preparing photocatalysts in which TiO_2 nanoparticles are located at the surface of a SiO_2 matrix, and thus fully accessible, while being stably immobilised and highly dispersed. In this synthesis method, the pre-formed TiO_2 nanoparticles are deposited on the surface of activated carbon, which then acts as hard template for the formation of a silica matrix embedding the nanoparticles (Scheme 1). Our synthesis method has another important asset: residual carbon and nitrogen atoms from the template and from the base used in the synthesis can lead to doping of the TiO_2 nanoparticles. Doping with non-metal elements as C, N, S or F has been reported as an efficient and cost-effective method to promote absorption of visible light by titanium dioxide photocatalysts [30–38]. Early reports proposed that N-doping modifies the electronic structure of TiO_2 through the mixing of N 2p and O 2p orbitals, with a consequent decrease in the band gap energy [39], but recent investigations showed that both carbon and nitrogen doping create intra-band-gap states that allow absorption in the visible region but do not modify the band gap [40–42]. Therefore, by combining nanostructuring of TiO_2, immobilisation at the surface of a silica matrix and engineering of the band gap by doping with C and N, we were able to tackle the major limitations of conventional TiO_2 and to produce a new class of photocatalysts with superior performance compared to the benchmark P25 TiO_2 under UV and, especially, visible radiation.

2. Experimental section

2.1. Materials

Titanium isopropoxide (TIP) and tetraethyl orthosilicate (TEOS) were purchased from Sigma-Aldrich and used as precursors for titanium dioxide and silica, respectively. Hydrochloric acid (aqueous HCl, 37 %) from Fischer Scientific was used for the synthesis of TiO_2 nanoparticles and aqueous ammonia (NH_3, 25 wt%) from Chem-Lab was used as base in the hydrolytic condensation of TEOS. The activated carbon used as sacrificial support and hard template was Norit SX1G, in powder form. Phenol (Sigma-Aldrich) and rhodamine B (Acros Organics) were used as the probe compounds in the photocatalytic tests. Milli-Q water with resistivity of 18.2 MΩ cm was employed for the preparation of the test solutions. All the chemicals were used without further purification.
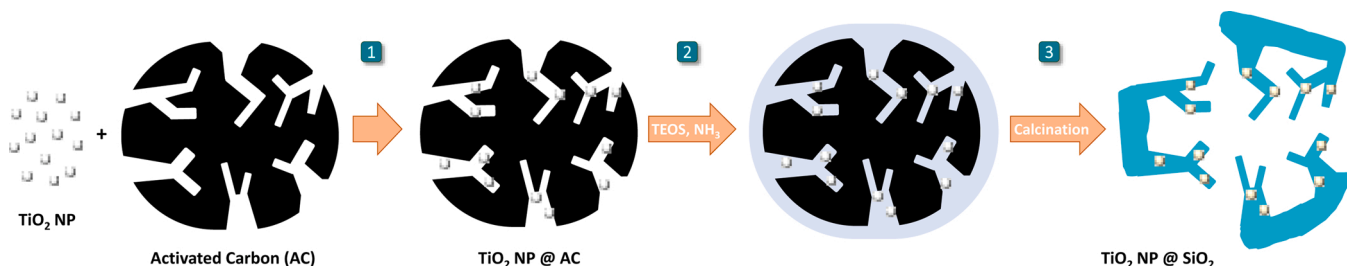
2.2. Synthesis procedures

2.2.1. TiO_2 nanoparticles

TiO_2 nanoparticles were prepared by hydrolysis of titanium isopropoxide in acidic H_2O/EtOH solution following a previously reported procedure [43]. Briefly, a solution of H_2O/EtOH = 130/40 (in volume) was prepared, acidified to pH = 1 with HCl 37 % (1.87 g) and heated up to 60 °C in a round-bottom flask equipped with a stirring bar and a reflux system. When the temperature stabilised at 60 °C, titanium isopropoxide (9.35 g) was added dropwise under vigorous stirring and allowed to react at 60 °C for 5 h. Then, the reflux system was removed and the temperature was increased to 80 °C to let the liquid evaporate slowly overnight. The final product was a fine white powder.

2.2.2. $TiO_2NP@SiO_2$ composites

A multistep procedure with activated carbon as hard template was used to produce a series of photocatalysts containing different TiO_2/SiO_2 weight ratios. First, the desired amount of the previously synthesised nanoparticles (between 26 and 360 mg) was suspended in 8 mL of H_2O/EtOH solution (3:1 volume ratio) and sonicated for at least 2 h to achieve a stable suspension. This TiO_2 suspension was then added to 3 g of activated carbon (Norit SX1G) by incipient wetness impregnation, followed by drying overnight in an oven at 80 °C. Then, 8 mL of a freshly prepared 0.5 M solution of TEOS in absolute ethanol was added by incipient wetness impregnation. The sample was again dried overnight in an oven at 80 °C. The final step consisted of adding 4 mL of 0.2 M aqueous solution of ammonia. The resulting wet powder was manually homogenised for 10 min. The material was kept at room temperature overnight and then dried in an oven at 80 °C for 24 h. Finally, the material was calcined at 550 °C for 6 h in air with heating rate of 2 °C/min. The produced photocatalysts were off-white powders denoted as X% $TiO_2NP@SiO_2$, where X% represents the theoretical weight percentage of TiO_2 (X = 10, 20, 30, 40, 50 and 60). It should be noted that the volume of the suspension containing the TiO_2 nanoparticles and that of the TEOS solution used in the synthesis method described above were

Scheme 1. Synthesis strategy to prepare photocatalysts with C- and N-doped TiO_2 nanoparticles embedded at the surface of a porous silica matrix ($TiO_2NP@SiO_2$). (1) A suspension containing TiO_2 nanoparticles is impregnated on activated carbon and dried. (2) TEOS is adsorbed in the pores of the carbon, followed by addition of NH_3 to promote the hydrolytic condensation of TEOS. (3) The activated carbon template is removed by calcination to obtain the $TiO_2NP@SiO_2$ composite photocatalysts.

kept equal and tuned to a specific value (8 mL), which was experimentally found to lead to the desired incipient wetness impregnation of the employed porous carbon template (*i.e.* complete absorption of the suspension/solution).

2.3. Characterisation

Transmission electron microscopy (TEM) images were recorded on a CM-200 FEG Philips equipment operating at 200 kV. Prior to analysis, the samples were suspended in ethanol and then deposited on 300-mesh carbon-coated copper grids. The chemical composition of the TiO_2-SiO_2 materials was determined by inductively coupled plasma optical emission spectroscopy (ICP-OES) on an Ultima Jobin Yvon emission instrument. Nitrogen physisorption measurements were performed on a Micromeritics Tristar 3000 apparatus and the surface area values were obtained by means of the BET method [44]. The crystalline phases present in the materials were studied by X-ray diffraction (XRD) on a high-throughput STOE Stadi P instrument with Cu Kα radiation (λ =1.5418 Å). The size of the TiO_2 nanoparticles was estimated by applying the Scherrer equation (without refinement) to the (101) peak of anatase ($\tau = K \lambda / \beta \cos\theta$, where τ is the average crystallite size, K is the shape factor taken as K = 0.9, β is the peak width at half height in radians and θ is the Bragg angle) [45]. Fourier-transform infrared (FT-IR) spectra were measured on a Nicolet 6700 spectrometer. Prior to analysis, the powder sample was mixed and ground with anhydrous KBr to obtain a pellet with 3 wt% of sample. Solid state UV–vis spectra were measured on a Varian Cary 5000 UV–vis spectrometer in diffusive reflectance configuration. The band gaps were evaluated with the Tauc plot method for an indirect transition [46]. In this method, the function $[F(R) h\nu]^{1/2}$ was plotted *vs.* hν (photon energy expressed in eV) and the band gap values were obtained from the extrapolation of the linear part of the function to the x-axis: the intercept corresponds to the band gap energy. F(R) is the Kubelka-Munk function defined as $F(R) = (1-R)^2/2R$, where R is the Reflectance (R = 1 - Absorbance). X-ray photoelectron spectroscopy (XPS) analysis was performed on a Physical Electronics PHI 1600 equipment using Al Kα (1486.6 eV) monochromatic X-ray source. The XPS signals were deconvoluted with Multipack software.

2.4. Photocatalytic tests

The degradation of phenol and rhodamine B in water were chosen as test reactions for this study (see Figs. 6 and 7 for the structural formulas of these probe compounds). These two compounds were selected for their different physicochemical properties (in terms of size, polarity, non-ionic *vs.* ionic nature) in order to evaluate the versatility of the TiO_2-based photocatalysts, while allowing for the complexity that can characterise the interpretation of the performance of photocatalysts in the degradation of dyes (as rhodamine B) [47]. For a typical photocatalytic test, 200 ppm (mg/L) solutions were prepared by dissolving either phenol or rhodamine B in Milli-Q water. 5 mL of the solution was added to a Pyrex test tube equipped with a stirring bar and in which 5 mg of photocatalyst had been added. First, the mixture was stirred in the dark for 1 h to achieve equilibrium between adsorption and desorption. Then, the irradiation period of 3 h was started (under stirring). In order to investigate if a longer adsorption time would cause a larger degree of adsorption, dark tests for 4 h were also carried out. Furthermore, kinetic tests with irradiation times of up to 16 h were performed, in which each data point in time was obtained from a separate experiment. All the photocatalytic tests were conducted in a high-throughput photoreactor (Fig. S1), which allows performing up to 16 tests simultaneously, with each test tube being individually stirred. The photoreactor was equipped with a rotating carousel and with 12 lamps (Hitachi FL8BL-B for UV radiation, and Sylvania cool white for visible light), which ensure homogeneous irradiation of all the samples, with two magnetic stirring plates and with a temperature controller set at 35 °C. The UV lamp irradiation spectrum consists of 98 % UV-A radiation with a minor

contribution from visible light and NIR ($\approx$ 2 %). The visible lamp irradiation spectrum consists of visible light ($\approx$ 90 %) with contributions of UV-A radiation ($\approx$ 6 %) and NIR ($\approx$ 4 %). The illuminance in the reactor was experimentally evaluated for both UV and visible radiation. The measurements were performed in 9 different positions inside the reactor and the readings were obtained after 3 min of equilibration. The illuminance was 9100 Lux (standard deviation of 1700 Lux) for UV radiation and 11700 Lux (standard deviation of 1400 Lux) for visible illumination. At the end of the test, the photocatalyst was separated by centrifugation (2000 rpm, 10 min) and the probe compound remaining in the supernatant was quantified. The degradation of rhodamine B was evaluated by UV–vis spectroscopy on a Perkin Elmer Lambda 12 UV–vis spectrophotometer. The maximum absorption at 550 nm was correlated to the residual concentration of dye in solution using Lambert-Beer law. Phenol was quantified by gas chromatography (GC) with tert-butanol as internal standard, which was added to the aqueous solution after separation of the catalyst. The GC analysis was performed on a Trace GC Ultra with Por. Q column and Ultra-Fast Module (UFM), which allows short analysis time ($\approx$ 5 min). The recycling tests were conducted employing double amount of photocatalyst (10 mg) compared to what normally used, to be able to deal with possible losses of material during the recycling procedure. At the end of each test, the material was washed with water (3 times, 5 mL), ethanol (3 times, 5 mL) and then dried overnight in an oven at 80 °C. Next, the photocatalyst was reused in a new test with a fresh solution of probe compound, following the procedure described above. The amount of solution used in each recycling test was corrected on the basis of the amount of catalyst recovered to keep the solution-to-catalyst ratio constant in all the tests. In parallel with the series of new photocatalysts, tests with P25 TiO_2 were conducted using the same experimental conditions. The use of this widely used, commercial photocatalyst provides a reliable benchmark to evaluate the photocatalytic activity of our materials. In the case of P25 TiO_2, higher centrifugation speed (3500 rpm, 10 min) was needed to achieve settling of the photocatalyst at the end of the tests.

3. Results and discussion

3.1. Synthesis and characterisation of the $TiO_2NP@SiO_2$ composites

A series of composite materials consisting of C- and N-doped TiO_2 nanoparticles embedded at the surface of a silica matrix was synthesised by employing activated carbon as hard template. The first step in the preparation of these TiO_2-SiO_2 composites involved the synthesis of TiO_2 nanoparticles, which were obtained by hydrolysis of titanium isopropoxide in water-ethanol medium acidified to pH = 1 with HCl. Low pH and ethanol are required to stabilise the nanoparticles and thus to obtain a stable suspension [48]. Characterisation with a combination of techniques confirmed that the desired TiO_2 nanoparticles were obtained. Notably, the low pH allows forming nanoparticles in anatase phase, though with low crystallinity, already at mild temperature (80 °C) and without any calcination treatment (Fig. 1.a; file 00-021-1272, PDF-2008) [49,50]. The small and broad peak at around $2\theta = 30°$ can be ascribed to the formation of brookite impurities (file 00-029-1360, PDF 2008). The size of the nanoparticles was estimated to be around 8 nm using the Scherrer equation [45]. In good agreement with this estimation, TEM images (Fig. 1.b) showed elongated particles with the major axis in the range of 6−8 nm and the minor axis in the range 4−6 nm. The TEM images also clearly showed lattice fringes with a spacing of *ca.* 0.35 nm, corresponding to the (101) planes of anatase [51]. The optical properties of the TiO_2 nanoparticles were determined by solid state UV–vis absorption spectroscopy (Fig. 1.c). The majority of the absorption lies in the UV region, with only a weaker absorption in the visible region, as expected for TiO_2. The band gap of the nanoparticles was evaluated using the Tauc plot method for an indirect transition (Fig. 1.d) [46]: the obtained value of 3.1 eV is slightly lower compared to the value reported for anatase (3.2 eV) [52]. This can be
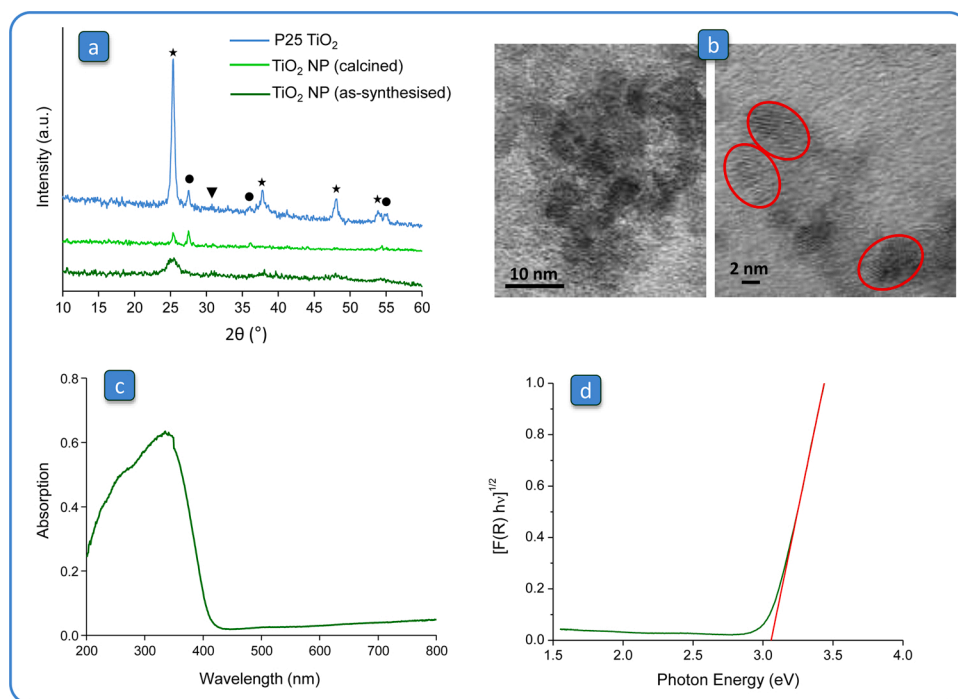
Fig. 1. TiO_2 nanoparticles characterisation: (a) Diffractograms of the as-synthesised nanoparticles, of the calcined nanoparticles and of P25 TiO_2. The diffractograms show the reflections of anatase (★), brookite (▼) and rutile (●); (b) TEM images of the TiO_2 nanoparticles (the red lines encircle individual nanoparticles); (c) Solid state UV–vis absorption spectrum of the as-synthesised nanoparticles; (d) Extrapolation of the band gap value using the Tauc plot method for an indirect transition. (For interpretation of the references to colour in this figure legend, the reader is referred to the web version of this article).

ascribed to the presence of the brookite phase together with the anatase main phase, as the former has a smaller band gap (3.1 eV) [50,52].

The prepared TiO_2 nanoparticles were employed to synthesise the target composite materials ($TiO_2NP@SiO_2$) using our novel synthesis method in which activated carbon has a multipronged role: as support to deposit the TiO_2 nanoparticles by incipient wetness impregnation from a water–ethanol suspension; as template for generating a silica matrix embedding the nanoparticles; and as source of C for doping TiO_2. Norit SX-1 G was chosen as activated carbon because of its high surface area (880 m^2/g) and its pore size distribution that includes pores in the micropore range (between 0.7 and 2 nm) and in the whole mesopore range, the latter being suitable for the adsorption of the TiO_2 nanoparticles [53,54]. The successive impregnation with TEOS fills the pore volume that is not occupied by the nanoparticles. The addition of an aqueous solution of ammonia promotes the hydrolysis and condensation of TEOS to produce the SiO_2 matrix embedding the TiO_2 nanoparticles. This synthesis method is designed to obtain a material in which the TiO_2 nanoparticles are sandwiched between the carbon and the SiO_2 phases

(Scheme 1). The final calcination step is necessary to burn off the carbon and produce a material in which the TiO_2 nanoparticles are stably embedded at the surface of the SiO_2 matrix, similarly to gems set on a ring. C and N residues provide the desired doping of the TiO_2 domains. The $TiO_2NP@SiO_2$ composite materials were prepared with different loading of TiO_2 nanoparticles ($X\%TiO_2NP@SiO_2$, with X = 10, 20, 30, 40, 50 and 60 wt% of TiO_2). Low-magnification TEM images (Fig. 2.a) of a representative material of the $TiO_2NP@SiO_2$ series (X = 50 wt%) showed the presence of the expected disordered distribution of pores, considering the above-mentioned porosity of the activated carbon template. The desired good dispersion of the TiO_2 nanoparticles in the SiO_2 matrix can be observed in the higher magnification TEM image (Fig. 2.b). The TiO_2 nanoparticles can be clearly identified by means of their crystal planes with the characteristic spacing of the (101) planes of anatase. The textural properties of the material were analysed by nitrogen physisorption. The isotherms can be described as type IV with H4 hysteresis loop, which are typical for mesoporous materials with slit-shaped pores (Fig. S2) [55], in agreement with the TEM analysis.
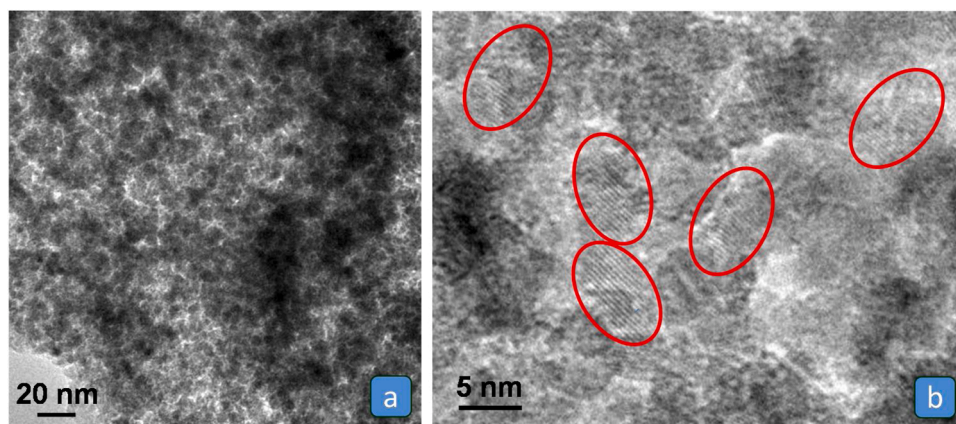

Fig. 2. TEM characterisation of $50\%TiO_2NP@SiO_2$: (a) Low-magnification image showing the porous structure of the titania/silica composite; (b) High-magnification image showing the presence of crystalline fringes and individual, well-dispersed nanoparticles. More TEM images are available in the supporting information (Fig. S5).

The BET surface areas of the composite materials range from 390 m^2/g for 10%TiO$_2$NP@SiO$_2$ to 295 m^2/g for 60%TiO$_2$NP@SiO$_2$ and show a gradual decrease with increasing amount of TiO$_2$ in the material (Table 1). This is partially due to the different atomic mass of titanium and silicon: increasing the relative amount of TiO$_2$ leads to a decreased specific surface area [56]. The surface areas of the TiO$_2$NP@SiO$_2$ materials are similar yet slightly lower compared to other previously reported TiO$_2$-SiO$_2$ systems [22,23]. On the other hand, the relative decrease in the surface area upon increase in TiO$_2$ loading is less marked than in the case of previous reported TiO$_2$-SiO$_2$ porous materials [25]. The pore size distribution evaluated from the adsorption branch is broad and is mainly in the mesopore region (Fig. S2), as expected considering that the materials are the negative replica of the activated carbon template. Most of the pore volume is due to mesoporosity, while micropores are either absent or account for a minor fraction ($<$ 8 %) of the total pore volume (Table 1).

The amount of TiO$_2$ incorporated in each composite material was determined by ICP-OES, showing an excellent agreement with the theoretical values (Table 1). These characterisation data show that the synthesis method is versatile in allowing to tune the loading of TiO$_2$ nanoparticles. The method is also robust and reproducible as shown by the consistent UV–vis spectra and photocatalytic activity when the synthesis of selected materials was repeated (data not shown). TiO$_2$ can crystallise in three polymorphs: anatase, rutile and brookite [58]. Rutile is the thermodynamically stable phase while anatase has been reported to be the most desirable phase for photocatalytic application [59]. XRD analysis of the series of TiO$_2$NP@SiO$_2$ composites (Fig. S3) showed in all cases the broad peak at 2θ = 25° corresponding to the (101) reflection of anatase, which was already detected in the diffractogram of the parent nanoparticles (Fig. 1.a). In line with logical expectations, the intensity of the peak increased with the amount of TiO$_2$ in the composite. The broadness of the signal indicates that the nanoparticles were not sintered during the synthesis even when a high fraction of TiO$_2$ (60 wt%) was present in the composite material. On the other hand, when the parent TiO$_2$ nanoparticles were calcined under the same conditions (550 °C), aggregation into large crystals occurred as indicated by the sharpening of the XRD peaks of anatase, coupled with the appearance of those of rutile (Fig. 1.a). These results underline the role of embedding the TiO$_2$ nanoparticles in the SiO$_2$ matrix in the TiO$_2$NP@SiO$_2$ materials in preventing agglomeration of the nanoparticles and in preserving their anatase structure [60,61].

Insights in the chemical environment surrounding the titanium atoms and on the band structure of the materials were obtained by solid state UV–vis spectroscopy (Fig. 3). The maximum absorption edge at 320 nm stems from Ti-O charge transfer for the octahedrally coordinated Ti atoms in TiO$_2$ [62]. Notably, the spectra of the TiO$_2$NP@SiO$_2$ composites present an absorption profile in the visible region (350–600 nm) that is totally absent in the spectrum of P25 TiO$_2$ (Fig. 3). This spectral feature is very similar to the absorption profile reported for TiO$_2$ materials doped with non-metal elements [63,64]. The intensity of the absorption in the visible region increased with decreasing TiO$_2$ content

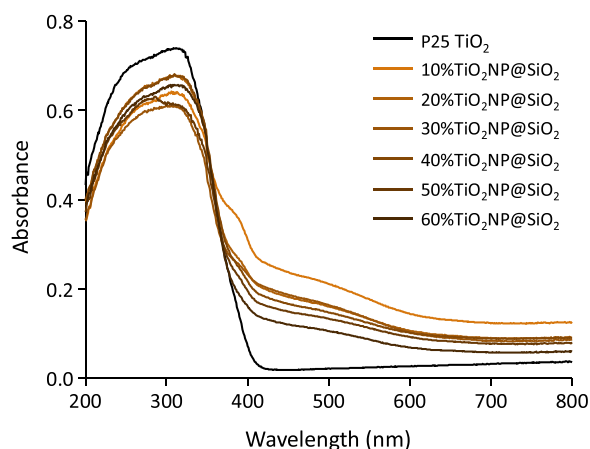**Fig. 3.** UV–vis absorption spectra of the TiO$_2$NP@SiO$_2$ materials and of P25 TiO$_2$.

in the composite material, reaching significantly higher intensity for 10%TiO$_2$NP@SiO$_2$ (Fig. 3). The appearance of these signals in the visible region of the spectra is ascribed to the presence of residual carbon and nitrogen in the composite materials [65]. The calculated band gaps (Table 1) are in line with the value of 3.2 eV commonly reported for anatase except for the material with 10 wt% of TiO$_2$, for which the band gap is close to 3.0 eV. This is a consequence of the higher intensity of the absorption band in the visible region (namely, the shoulder at ≈ 400 nm). However, it should be kept in mind that recent studies showed that doping TiO$_2$ with carbon or nitrogen does not modify the band gap of the material but enhances the visible response because of the formation of inter-band-gap states [40–42]. The presence of C and N atoms in the TiO$_2$-SiO$_2$ composite materials was further monitored by elemental analysis of the surface by XPS. 20%TiO$_2$NP@SiO$_2$ was chosen as representative material for this analysis because it has a clear absorption band in the visible region together with a sufficiently high fraction of TiO$_2$. The full-scan spectrum of 20%TiO$_2$NP@SiO$_2$ (Fig. S4 in the SI) shows the presence of Si, Ti, O, C and N. The concentration of C and N determined by XPS was 4 at% and 1 at%, respectively. The deconvolution of the O 1s signal (Fig. 4.a) gives three components corresponding to three different oxygen environments: Si-O-Si (BE = 533.8 eV), Ti-O-Ti (530.8 eV) and a third peak at 532.5 eV, which has been assigned to Si-O-Ti or to surface hydroxyls (or a combination of the two) [66,67]. O species bound to C are also expected to be present in the material in small amounts (*vide infra*), but the signals of -CO$_2$H groups (at around 534 eV) of C-OH bonds in phenols (at around 533 eV) and of C=O groups (at around 531−532 eV) [68] cannot be discerned from those of the Si-O and Ti-O species. Titanium gives the expected Ti 2p$_{3/2}$ and Ti 2p$_{1/2}$ peaks. The Ti 2p$_{3/2}$ signal (Fig. 4.b) can be deconvoluted in two peaks (BE = 459 eV and BE = 458 eV), corresponding to two different titanium species: Ti^{4+} and Ti^{3+}, respectively [67]. The

Table 1
Physicochemical properties of the synthesised TiO$_2$NP@SiO$_2$ composites.

Photocatalyst	BET surface area (m^2/g) [a]	Total pore volume (cm^3/g) [a]	Micropore volume (cm^3/g) [a]	Band gap (eV) [b]	TiO$_2$ content (wt%) [c]
10%TiO$_2$NP@SiO$_2$	390	0.37	0.03	3.02	8
20%TiO$_2$NP@SiO$_2$	380	0.36	0.02	3.20	21
30%TiO$_2$NP@SiO$_2$	375	0.36	0.02	3.18	29
40%TiO$_2$NP@SiO$_2$	315	0.36	0	3.17	41
50%TiO$_2$NP@SiO$_2$	320	0.39	0	3.17	49
60%TiO$_2$NP@SiO$_2$	295	0.37	0	3.22	61
P25 TiO$_2$	55[d]	–	–	3.13	–

[a] Determined by N$_2$ physisorption.
[b] Determined by applying the Tauc plot method for an indirect transition to the UV–vis absorbance data.
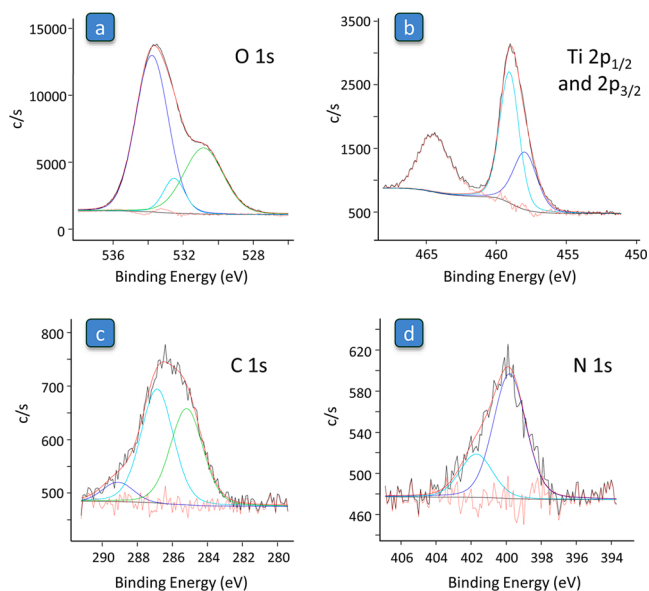[c] Determined by ICP-OES.
[d] From reference [57].

Fig. 4. Narrow-scan XPS signals of 20%TiO₂NP@SiO₂ for the most relevant elements, with their deconvolution: (a) O 1s, (b) Ti 2p$_{1/2}$ and Ti 2p$_{3/2}$, (c) C 1s, (d) N 1s.

presence of Ti^{3+} is often reported when TiO₂ is synthesised in the presence of reducing agents such as the carbon used as support in this work [69]. The low intensity C 1s and N 1s signals were deconvoluted to identify the configuration of each of the two doping elements. The C 1s signal (Fig. 4.c) comprises three different peaks: two main peaks at 284.9 and 286.6 eV and a smaller peak at 289.1 eV. The first peak stems from graphitic carbon, whereas the last two peaks indicate partially oxidised carbon species (*i.e.* alcohol, ether or carbonyl species for the peak at 286.6 eV and carboxyl groups or carbonate species for the peak at 289.1 eV) [68]. Similar C 1s signals have been reported in the literature for C-doped TiO₂ prepared by hydrolysis of titanium tetrachloride with tetrabutylammonium hydroxide, followed by calcination at mild temperature [65]. It has been proposed that these oxidised carbons species derive from carbon doping at interstitial position in the TiO₂ structure, in which carbon is stabilised by oxygen atoms [15]. The N 1s signal (Fig. 4.d) is in the typical range from 396 to 404 eV [39,70], and can be deconvoluted in two peaks centred at 399.2 and 401.5 eV. The position of these peaks corresponds to N atoms in largely covalent bonds as those found in N-doped carbon materials (such as N in pyridinic, pyrrolic or graphitic configuration) [71] and differs from that of nitride species (BE = 397 eV) [72], or of nitrites and nitrates inserted interstitially in the TiO₂ structure (BE = 407−408 eV) [71,73].

The characterisation study was completed by FT-IR analysis (Fig. 5) of two representative materials of the TiO₂NP@SiO₂ series. The FT-IR spectra of 10%TiO₂NP@SiO₂ and 50%TiO₂NP@SiO₂ exhibit the characteristic features of TiO₂-SiO₂ composites [74,75]. The broad band centred at around 3400 cm^{-1} (●) and the signal at 1630 cm^{-1} (★), derive from stretching and bending of surface hydroxyls, respectively. The intense, complex band in the 980−1260 cm^{-1} range is due to Si-O-Si symmetric stretching (▲), whereas the low-intensity band at 790 cm^{-1} arises from asymmetric stretching of Si-O-Si species (■). The signal at 460 cm^{-1} can be assigned to rocking of Si-O-Si or, alternatively, to the bending mode of Ti-O groups (▼). Ti-O-Ti stretching (△) gives a broad band centred at 700 cm^{-1}, which is more intense in the spectrum of 50% TiO₂NP@SiO₂ than in the one of 10%TiO₂NP@SiO₂, in line with logical expectations. The Si-O-Ti species anticipated by XPS is confirmed by the presence of the low intensity band at 939 cm^{-1}, which corresponds to the stretching mode of this group (*) [74]. Finally, the group of signals in the range 3000−2800 cm^{-1} indicates the C–H stretching due to residual organic species (□).
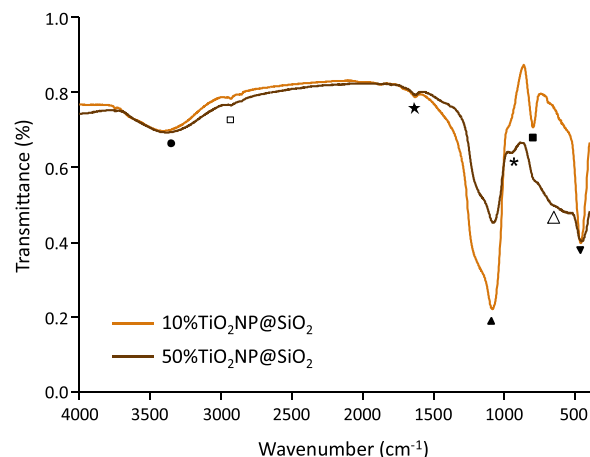

Fig. 5. FT-IR spectra (3 wt% in KBr) of 10%TiO₂NP@SiO₂ and 50%TiO₂N-P@SiO₂ in the region 400−4000 cm^{-1}. Symbols refer to: stretching (●) and bending (★) of surface hydroxyls; symmetric (▲) and asymmetric (■) stretching of Si-O-Si; Si-O-Si rocking or Ti-O bending (▼); Ti-O-Ti stretching (△); Si-O-Ti stretching (*); C–H stretching (□).

3.2. Photocatalytic performance of the TiO₂NP@SiO₂ materials

The photocatalytic activity of the TiO₂NP@SiO₂ materials in the degradation of pollutants was performed under both UV and visible radiation employing rhodamine B (RhB) and phenol as probe compounds, which were selected for their complementary features: RhB is a bulky, ionic compound that can absorb radiation in the visible region (and is thus used as a dye), whereas phenol is a smaller, non-ionic molecule with no significant absorption in the visible region. First, the adsorption capacity of the TiO₂NP@SiO₂ materials in the dark was measured for 1 h and 4 h. Only minor differences between the adsorption tests conducted for 1 and 4 h were found, which means that the adsorption-desorption equilibrium is nearly reached after 1 h of stirring in the dark. In line with logical expectations, the removal of the probe compounds by adsorption increased with the surface area of the materials (Figs. 6 and 7). The adsorption capacity of the TiO₂NP@SiO₂ materials is significantly higher compared to previously reported TiO₂–SiO₂ structured photocatalysts with comparable surface areas [25]. This difference is attributed to the nature of the pores in the TiO₂NP@SiO₂ materials, which in mainly in the mesopore range with only a minor contribution of micropores (Table 1). This minimises diffusion
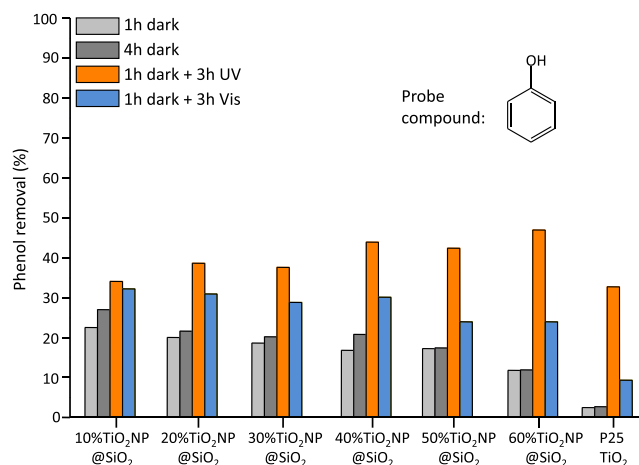

Fig. 6. Adsorption and photocatalytic degradation of phenol under UV and visible radiation with the series of TiO₂NP@SiO₂ composites and P25 TiO₂. Conditions: 5 mg of photocatalyst (1 mg/mL), 200 ppm (200 mg/L) of phenol. The tests were performed at 35 °C in aerobic conditions.
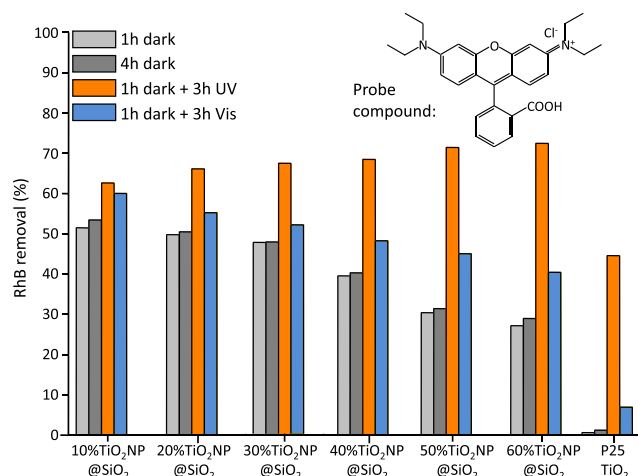
Fig. 7. Adsorption and photocatalytic degradation of rhodamine B under UV and visible radiation with the series of TiO$_2$NP@SiO$_2$ composites and P25 TiO$_2$. Conditions: 5 mg of photocatalyst (1 mg/mL), 200 ppm (200 mg/L) of RhB. The tests were performed at 35 °C in aerobic conditions.

limitations and leads to an efficient adsorption of the two probe compounds. The benchmark P25 TiO$_2$ showed poor adsorption capacity towards the probe compounds due to its lower surface area compared to the TiO$_2$NP@SiO$_2$ composites, and its non-porous nature allowed it to approach the adsorption-desorption equilibrium after 1 h in the dark.

In the series of photocatalytic tests conducted with phenol and RhB, both under UV and visible radiation, the activity shown by the TiO$_2$NP@SiO$_2$ materials is remarkable: all the photocatalysts are able to remove higher amount of polluting agent from the aqueous solution compared to the P25 TiO$_2$ benchmark (Figs. 6 and 7). This enhanced performance is ascribed to the new strategy employed for the synthesis of the porous TiO$_2$NP@SiO$_2$ materials with the purpose of embedding the TiO$_2$ nanoparticles at the surface of the photocatalyst (as shown by TEM, Fig. 2), thus maximising their accessibility and, therefore, their photocatalytic activity. Additionally, the firm immobilisation of the TiO$_2$ nanoparticles at the surface of the silica matrix ensures stability against aggregation during the reaction (which, on the other hand, is a known issue for P25 TiO$_2$) [76]. Another important contribution to this result is provided by the increased adsorption capacity of the porous TiO$_2$NP@SiO$_2$ materials compared to P25 TiO$_2$ (stemming from their higher specific surface areas, see Table 1), which favours the accumulation of pollutants on the surface of the photocatalysts where the concentration of photogenerated reactive oxygen species is higher and which concomitantly promotes the direct interaction of the probe compounds with the electron-hole couple [10]. Finally, the C- and N-doping demonstrated by XPS and UV–vis absorption (Figs. 3 and 4) bestows enhanced photocatalytic activity under visible light.

Taking into consideration the combination of adsorption capacity and photocatalytic activity, 60%TiO$_2$NP@SiO$_2$ shows the best performance in the removal of probe compounds from the water solution with UV radiation. The importance of embedding the TiO$_2$ nanoparticles at the surface of the silica matrix is further confirmed by the much higher photocatalytic activity of 60%TiO$_2$NP@SiO$_2$ compared to the unsupported nanoparticles (1 % removal of RhB after 1 h in the dark, 27 % removal after further 3 h UV irradiation under the same conditions used in the tests in Fig. 7). Although the adsorption capacity decreases with increasing TiO$_2$ content in the TiO$_2$NP@SiO$_2$ series, the removal of both probe compounds under UV radiation follows an overall increasing trend by increasing the amount of TiO$_2$ active phase (Figs. 6 and 7). This result contrasts with previously reported TiO$_2$-SiO$_2$ photocatalysts, with which the removal of the probe compounds reached the maximum at intermediate TiO$_2$ content [25]. The different behaviour of the TiO$_2$NP@SiO$_2$ materials is ascribed to the milder loss of surface area upon

increase in TiO$_2$ loading and to the enhanced accessibility of the TiO$_2$ nanoparticles in these photocatalysts. The photocatalytic performance of the TiO$_2$NP@SiO$_2$ materials under visible light follows a completely different trend than under UV radiation, with the highest removal being obtained with 10%TiO$_2$NP@SiO$_2$, both with phenol and rhodamine B as probe compound (Figs. 6 and 7). This is due to the combination of two factors: (i) as shown by the UV–vis spectra (Fig. 3), 10%TiO$_2$NP@SiO$_2$ displayed the most intense absorption in the visible range in the series of photocatalysts; (ii) since the photocatalytic activity is lower when using visible instead of UV radiation [30], the contribution of the adsorption of the probe on the surface of the photocatalyst becomes more important (10%TiO$_2$NP@SiO$_2$ has the highest surface area in the series). For practical application in water purification, the effective amount of probe compound that is removed from the solution (Figs. 6 and 7) represents the most important figure for evaluating the performance of the photocatalysts. On the other hand, more insight into the strictly photocatalytic activity of the materials can be obtained by calculating the turnover numbers (TON) on the basis of the amount of probe compound removed from the solution after 3 h of irradiation, from which the amount of probe removed during the initial 1 h of adsorption in the dark was subtracted [25]. The analysis of the TON values for the tests under UV and visible radiation (Figs. 8 and 9) shows that all the synthesised materials display higher activity than the P25 TiO$_2$ benchmark. This excellent result becomes even more remarkable when observing that the TON obtained over the TiO$_2$NP@SiO$_2$ photocatalysts are also significantly higher than those found with previously reported TiO$_2$-SiO$_2$ porous photocatalytic systems with the same TiO$_2$ loading (Table S1). This result is ascribed to the novel synthesis strategy used in this work, which was designed to obtain materials in which the TiO$_2$ nanoparticles are located at the surface and thus available for the photocatalytic reaction, whereas in the TiO$_2$-SiO$_2$ photocatalysts reported in the literature the active TiO$_2$ phase is located both at the surface of the materials and in inaccessible domains in the bulk of the materials [22,23,25]. The fact that the specific surface areas of our TiO$_2$ NP@SiO$_2$ materials are in the same range as for the literature TiO$_2$-SiO$_2$ porous photocatalysts with the same TiO$_2$ content supports the hypothesis that the enhanced photocatalytic activity of the TiO$_2$NP@SiO$_2$ materials stems from the higher accessibility of the active TiO$_2$ phase provided by our photocatalyst design. The beneficial effect of dispersing the TiO$_2$NP@SiO$_2$ nanoparticles at the surface of the SiO$_2$ matrix is highlighted by the fact that the TON values are higher for materials with lower TiO$_2$ content: 10%TiO$_2$NP@SiO$_2$ displayed the highest TON in the degradation of phenol under visible light and in the degradation of rhodamine B both
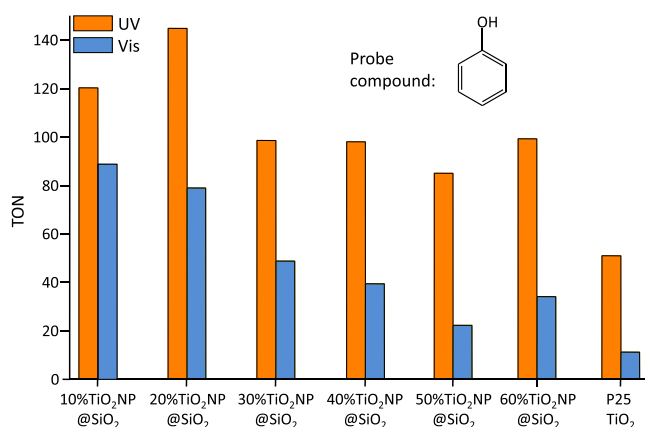

Fig. 8. TON values for the degradation of phenol with TiO$_2$NP@SiO$_2$ as photocatalysts under UV or visible light radiation. TON = mmol of substrate degraded/mol of TiO$_2$. The mmol of substrate degraded are calculated by subtracting the mmol of substrate adsorbed during the test in the dark from the mmol of substrate removed from the solution at the end of the photocatalytic test.
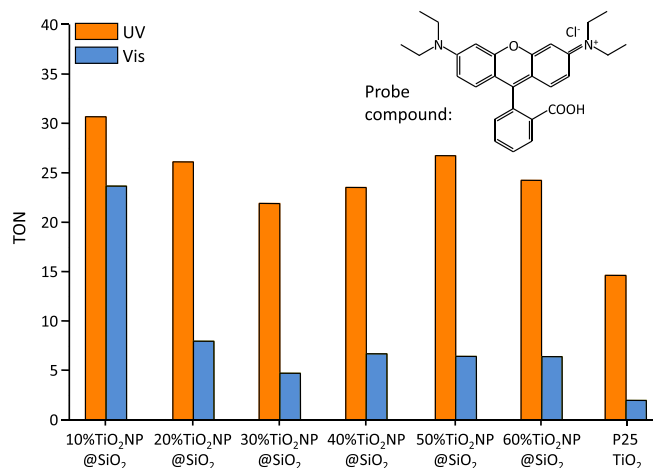
Fig. 9. TON values for the degradation of rhodamine B with TiO$_2$NP@SiO$_2$ as photocatalysts under UV or visible light radiation. TON = mmol of substrate degraded/mol of TiO$_2$. The mmol of substrate degraded are calculated by subtracting the mmol of substrate adsorbed during the test in the dark from the mmol of substrate removed from the solution at the end of the photocatalytic test.

Table 2
Comparison between the TON values of the TiO$_2$NP@SiO$_2$ photocatalysts and those of P25 TiO$_2$ in the degradation of phenol and rhodamine B under UV and visible radiation.

| Photocatalyst | TON$_{TiO2NP@SiO2}$/TON$_{P25TiO2}$ | | | |
| | Phenol | | Rhodamine B | |
	UV	Vis	UV	Vis
10%TiO$_2$NP@SiO$_2$	2.4	7.9	2.1	12.2
20%TiO$_2$NP@SiO$_2$	2.8	7.0	1.8	4.1
30%TiO$_2$NP@SiO$_2$	1.9	4.3	1.5	2.4
40%TiO$_2$NP@SiO$_2$	1.9	3.5	1.6	3.4
50%TiO$_2$NP@SiO$_2$	1.7	2.0	1.8	3.3
60%TiO$_2$NP@SiO$_2$	1.9	3.0	1.6	3.3

with UV and visible radiation, whereas 20%TiO$_2$NP@SiO$_2$ showed the highest TON in the degradation of phenol under UV radiation. The TON values also allow evaluating in more detail the activity of the TiO$_2$N-P@SiO$_2$ photocatalysts under visible light. It is well known that P25 TiO$_2$ has low photocatalytic activity under visible light due to its large band gap value of around 3.1 eV (Table 1). This is reflected by its very low TON values and by the small amount of probe compound removed

in the tests under visible light (Figs. 6–9) [77]. On the other hand, the carbon and nitrogen doping of the TiO$_2$ nanoparticles observed in the TiO$_2$NP@SiO$_2$ materials enhanced their absorption of visible light (*vide supra*). The effect of this doping on the photocatalytic activity under visible light is evidenced by the comparison of the TON of the TiO$_2$N-P@SiO$_2$ materials with those of P25 TiO$_2$ (Table 2). The TON$_{TiO2N-P@SiO2}$/TON$_{TiO2P25}$ ratio is consistently higher under visible light than under UV radiation, indicating that the doping contributes to a further improvement of the photocatalytic performance of the TiO$_2$NP@SiO$_2$ materials compared to P25 TiO$_2$. The gain in activity with visible light is particularly impressive for 10% and 20%TiO$_2$NP@SiO$_2$ (Table 2), *i.e.* for the materials that showed the highest intensity in the absorption of radiation in the visible range (Fig. 3), with the TON over 10%TiO$_2$N-P@SiO$_2$ under visible light being around one order of magnitude higher than over P25 TiO$_2$ (TON$_{10\%TiO2NP@SiO2}$/TON$_{TiO2P25}$ = 7.9 with phenol and TON$_{10\%TiO2NP@SiO2}$/TON$_{TiO2P25}$ = 12.2 with RhB). It is worth noting that, although the high TON values achieved with 10%TiO$_2$NP@SiO$_2$ in the photocatalytic degradation of phenol and rhodamine B are very promising, they are still slightly lower compared to those obtained with the same material under UV radiation. This is in line with previous reports and has been attributed to the discrete nature of the intra-band-gap states created by nitrogen and carbon doping, which limits the mobility of the generated electron-hole couples compared to the case in which these are formed in the conduction and valence bands [30,78]. When comparing the TON$_{TiO2NP@SiO2}$/TON$_{TiO2P25}$ ratios for the degradation of phenol with those for rhodamine B, on average no major differences are observed between the two probe compounds, both under UV and visible radiation (Table 2). Particularly, the fact that the relative increase of TON compared to P25 TiO$_2$ under visible radiation with rhodamine B is on average similar to that with phenol supports the hypothesis that the observed activity of the TiO$_2$NP@SiO$_2$ photocatalysts under visible radiation mainly stems from the doping of the materials rather than being caused by sensitisation induced by the rhodamine B dye.

The study of the photocatalytic properties of the new composite materials was broadened with an investigation of the kinetics of the degradation of phenol and rhodamine B under UV and visible radiation with 50%TiO$_2$NP@SiO$_2$ as the photocatalyst (Fig. 10). In parallel, the kinetics of the adsorption in the dark was followed for the whole reaction time, confirming that the equilibrium between adsorption and desorption is (nearly) achieved during the first hour. In the tests performed under UV radiation, complete removal of the dye was achieved after 18 h, whereas under the same conditions a small amount of phenol was still present in the aqueous solution (81 % removal). It should be noted that even if the removal of rhodamine B was complete, its photocatalytic degradation occurs at a lower rate compared to that of phenol
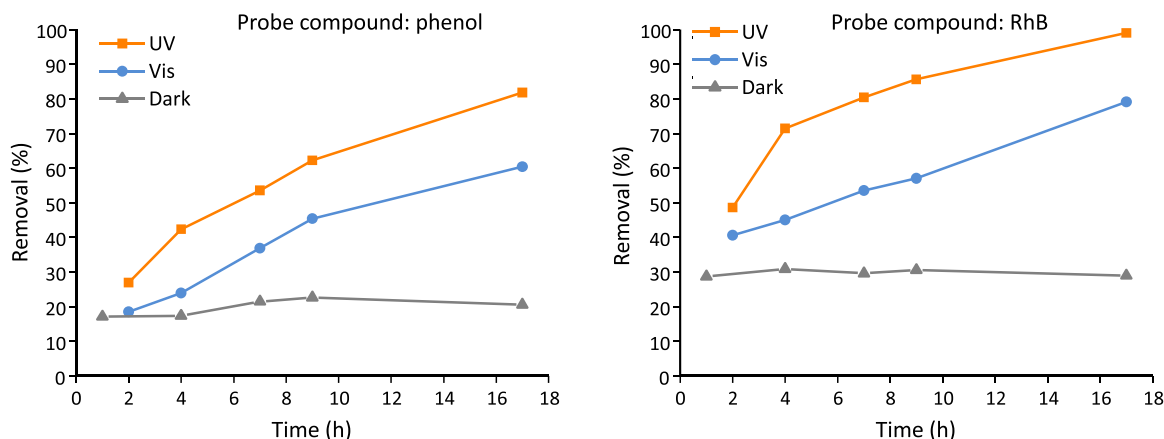

Fig. 10. Kinetic tests with phenol (left) and rhodamine B (right) as probe compounds and 50%TiO$_2$NP@SiO$_2$ as photocatalyst. The adsorption properties and the photocatalytic degradation are studied over the course of 18 h. In all cases, the first hour of the test was in the dark. Conditions: 5 mg of photocatalyst (1 mg/mL), 200 ppm (200 mg/L) of probe compound. The tests were performed at 35 °C in aerobic conditions.
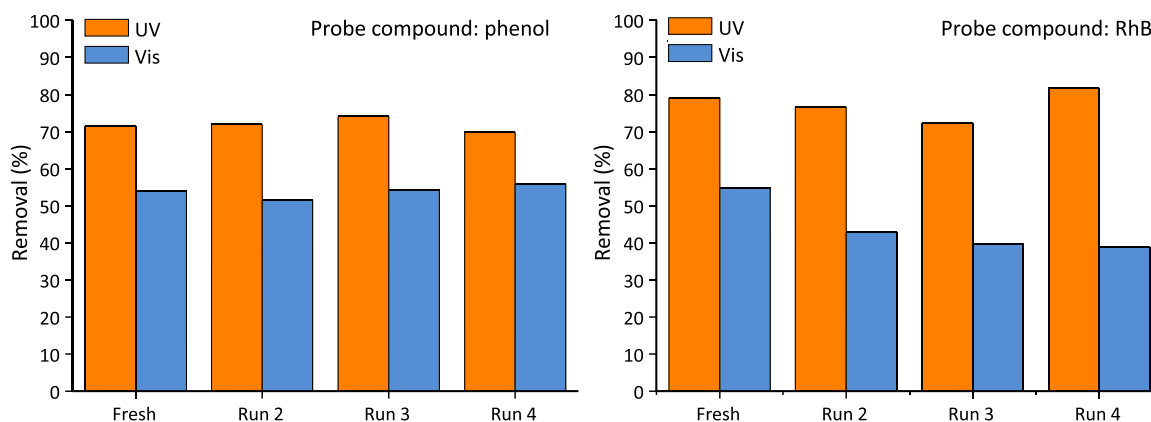
Fig. 11. Recycling tests with 50%TiO₂NP@SiO₂ as photocatalyst and phenol (left) or rhodamine B (right) as probe compounds. Conditions: 10 mg 50%TiO₂N-P@SiO₂, 5 mL of 200 ppm probe compound water solution. The mixture was stirred 1 h in the dark and then the irradiation proceeded for further 3 h. The tests were performed at 35 °C in aerobic conditions.

(see also the TON values in Figs. 8 and 9). This becomes evident when considering that the tests were performed with the same mass of probe compound, and thus with a much higher number of moles of phenol. The tests conducted with visible light showed slower removal of phenol and rhodamine B compared to the tests performed with UV radiation, in line with the previous tests (Figs. 6 and 7). Under these conditions, the removal of phenol reached 60 % after 18 h, whereas 79 % of rhodamine B was removed in the same time [79]. Since no plateaus were observed in the removal values for the dye and for phenol over long irradiation periods, it is reasonable to expect that complete degradation of the probe compounds can be achieved over the TiO₂NP@SiO₂ photocatalysts with longer reaction time or higher photocatalyst loading.

Since the design of the TiO₂NP@SiO₂ photocatalysts should grant the firm immobilisation of the TiO₂ nanoparticles at the surface of the silica matrix, a high stability of the material is expected. To check if this was the case, the reusability of 50%TiO₂@SiO₂ in successive runs was tested (Fig. 11). The tests were performed both under UV and visible radiation. The latter test also addressed the stability of the doping species present in the photocatalyst [80,81]. In the degradation of phenol, 50%TiO₂N-P@SiO₂ showed an excellent recyclability both under UV and visible radiation. Compared to reusability tests of P25 TiO₂ in the degradation of phenol under UV radiation [25], our 50%TiO₂NP@SiO₂ photocatalyst displayed similar retention of the original activity (per gram of material) upon recycling, but was easier to separate and recover from the reaction mixture. In the case of the degradation of RhB, the activity of the photocatalyst was retained upon recycling for the tests under UV radiation, whereas a gradual, slight decrease in the activity (particularly between the first and the second run) was observed under visible radiation. This is attributed to the combination of the less efficient degradation process under visible light and the strong adsorption of the dye on the surface of the material, as indicated by the fact that the material was still coloured at the end of the test.

4. Conclusions

A new synthesis strategy was developed for the production of highly active TiO₂/SiO₂ photocatalysts consisting of accessible C- and N-doped TiO₂ nanoparticles embedded at the surface of a porous silica matrix. In order to achieve this material, pre-prepared TiO₂ nanoparticles were deposited on the surface of activated carbon, followed by impregnation with TEOS and ammonia to produce a porous silica matrix as negative copy of the carbon material. The activated carbon template was then removed by calcination to obtain the production of the target TiO₂N-P@SiO₂ materials. The synthesised materials were tested in the photocatalytic degradation of pollutants (phenol and rhodamine B) under UV and visible radiation showing significantly higher activity than the

benchmark P25 TiO₂, both in terms of removal % and turnover numbers. Residual carbon and nitrogen from the synthesis procedure were characterised by XPS and were found responsible for the excitation of TiO₂NP@SiO₂ materials with visible radiation. The high specific surface area, the accessibility and the stability of the TiO₂ nanoparticles that were demonstrated by N₂ physisorption, TEM and XRD, were identified as the crucial factors leading to the increased photocatalytic activity of the TiO₂NP@SiO₂ materials compared to the benchmark photocatalyst. The increase in photocatalytic activity compared to P25 TiO₂ was even more remarkable in the tests conducted under visible light, as a consequence of the doping of the TiO₂ nanoparticles with carbon and nitrogen atoms. Particularly, the 10%TiO₂NP@SiO₂ photocatalyst achieved highly enhanced TON values in the degradation of rhodamine B and phenol under visible radiation (the TON was 12 times that of P25 TiO₂ for RhB, and 8 times that of P25 TiO₂ for phenol). The photocatalysts are easier to recover than P25 TiO₂ and can be efficiently reused. Importantly, the novel synthesis method is also robust, straightforward and relatively inexpensive, as no costly structure directing agent is required for generating the high surface area materials. Moreover, the synthesis strategy has the potential for being extended to other catalytically relevant metal oxides nanoparticles.

CRediT authorship contribution statement

Damiano Cani: Investigation, Methodology, Formal analysis, Validation, Data curation, Writing, Visualization. **Jan C. van der Waal:** Conceptualization, Methodology, Writing. **Paolo P. Pescarmona:** Conceptualization, Methodology, Formal analysis, Supervision, Writing, Visualization, Funding acquisition, Project administration.

Declaration of Competing Interest

The authors report no declarations of interest.

Acknowledgements

Appendix A. Supplementary data

Supplementary material related to this article can be found, in the online version, at doi:https://doi.org/10.1016/j.apcata.2021.118179.

References

[1] A. Fujishima, K. Honda, Nature 238 (1972) 37.
[2] J. Herrmann, Catal. Today 53 (1999) 115.
[3] M.S. Hamdy, W.H. Saputera, E.J. Groenen, G.J. Mul, J. Catal. 310 (2014) 75.
[4] D. Chen, Y. Cheng, N. Zhou, P. Chen, Y. Wang, K. Li, S. Huo, P. Cheng, P. Peng, R. Zhang, L. Wang, H. Liu, Y. Liu, R. Ruana, J. Clean. Prod. 268 (2020), 121725.
[5] I.K. Konstantinou, T.A. Albanis, Appl. Catal. B 49 (2004) 1.
[6] S.E. Braslavsky, A.M. Braun, A.E. Cassano, A.V. Emeline, M.I. Litter, L. Palmisano, V.N. Parmon, N. Serpone, Pure Appl. Chem. 83 (2011) 931.
[7] A. Kubacka, M. Fernández-García, G. Colón, Chem. Rev. 112 (2012) 1555.
[8] J. Schneider, M. Matsuoka, K. Takeuchi, J. Zhang, Y. Horiuchi, M. Anpo, D. W. Bahnemann, Chem. Rev. 114 (2014) 9919.
[9] V. Augugliaro, M. Bellardita, V. Loddo, G. Palmisano, L. Palmisano, S.J. Yurdakal, Photochem. Photobiol. C Photochem. Rev. 13 (2012) 224.
[10] A. Khadem-Hosseini, S.M. Mirabedini, S.J. Pazokifard, J. Mater. Sci. 51 (2016) 3219.
[11] Q.A. Naqvi, M. Ratova, R. Klaysri, P.J. Kelly, M. Edge, S. Potgieter-Vermaak, L. Tosheva, Catal. Today 326 (2019) 54.
[12] S. Horikoshi, N. Serpone, Catal. Today 340 (2020) 334.
[13] R. López, R. Gómez, J. Solgel Sci. Technol. 61 (2012) 1.
[14] M. Woodhouse, B.A. Parkinson, Chem. Soc. Rev. 38 (2009) 197.
[15] T. Peng, D. Zhao, K. Dai, W. Shi, K. Hirao, J. Phys. Chem. B 109 (2005) 4947.
[16] T. Tachikawa, M. Fujitsuka, T.J. Majima, Phys. Chem. C 111 (2007) 5259.
[17] F. Han, V.S.R. Kambala, M. Srinivasan, D. Rajarathnam, R. Naidu, Appl. Catal. A 359 (2009) 25.
[18] W. Fu, G. Li, Y. Wang, S. Zeng, Z. Yan, J. Wang, S. Xin, L. Zhang, S. Wu, Z. Zhang, Chem. Commun. 54 (2018) 58.
[19] A.R. Khataee, M.N. Pons, O. Zahraa, J. Hazard. Mater. 168 (2009) 451.
[20] A.Y. Shan, T.I.M. Ghazi, S.A. Rashid, Appl. Catal. A 389 (2010) 1.
[21] X. Collard, A. Comès, C. Aprile, Catal. Today 241 (2015) 33.
[22] M. Alvaro, C. Aprile, M. Benitez, E. Carbonell, H. García, J. Phys. Chem. B 110 (2006) 6661.
[23] J. Jammaer, C. Aprile, S.W. Verbruggen, S. Lenaerts, P.P. Pescarmona, J. A. Martens, ChemSusChem 4 (2011) 1457.
[24] D.S. Gopala, R.R. Bhattacharjee, R. Haerr, B. Yeginoglu, O.D. Pavel, B. Cojocaru, V. I. Parvulescu, R.M. Richards, ChemCatChem 3 (2011) 408.
[25] D. Cani, P.P. Pescarmona, J. Catal. 311 (2014) 404.
[26] X. Collard, M. El Hajj, B.L. Su, C. Aprile, Microporous Mesoporous Mater. 184 (2014) 90.
[27] D. Maučec, A. Šuligoj, A. Ristić, G. Dražić, A. Pintar, N. Novak Tušar, Catal. Today 310 (2018) 32.
[28] J. Fernández-Catalá, D. Cazorla-Amorós, Á. Berenguer-Murcia, Appl. Catal. A 564 (2018) 123.
[29] A. Lolli, M. Blosi, S. Ortelli, A.L. Costa, I. Zanoni, D. Bonincontro, F. Carella, S. Albonetti, Catal. Today 334 (2019) 193.
[30] M. Pelaez, N.T. Nolan, S.C. Pillai, M.K. Seery, P. Falaras, A.G. Kontos, P.S. M. Dunlop, J.W.J. Hamilton, J.A. Byrne, K. O'Shea, M.H. Entezari, D.D. Dionysiou, Appl. Catal. B 125 (2012) 331.
[31] D. Chatterjee, S. Dasgupta, J. Photochem. Photobiol. C Photochem. Rev. 6 (2005) 186.
[32] D. Chen, Z. Jiang, J. Geng, Q. Wang, D. Yang, Ind. Eng. Chem. Res. 46 (2007) 2741.
[33] A.M. Czoska, S. Livraghi, M. Chiesa, E. Giamello, S. Agnoli, G. Granozzi, E. Finazzi, C. Di Valentin, G. Pacchioni, J. Phys. Chem. C 112 (2008) 8951.
[34] B. Cojocaru, Ş. Neaţu, V.I. Pârvulescu, V. Şomoghi, N. Petrea, G. Epure, M. Alvaro, H. Garcia, ChemSusChem 2 (2009) 427.
[35] U.G. Akpan, B.H. Hameed, Appl. Catal. A 375 (2010) 1.
[36] C. Han, M. Pelaez, V. Likodimos, A.G. Kontos, P. Falaras, K. O'Shea, D. D. Dionysiou, Appl. Catal. B 107 (2011) 77.
[37] J. Shao, W. Sheng, M. Wang, S. Li, J. Chen, Y. Zhang, S. Cao, Appl. Catal. B 209 (2017) 311.
[38] I. Barba-Nieto, U. Caudillo-Flores, M. Fernandez-Garcia, A. Kubacka, Molecules 25 (2020) 4008.
[39] R. Asahi, T. Morikawa, T. Ohwaki, K. Aoki, Y. Taga, Science 293 (2001) 269.
[40] S. Livraghi, M.C. Paganini, E. Giamello, A. Selloni, C. Di Valentin, G. Pacchioni, J. Am. Chem. Soc. 128 (2006) 15666.
[41] C. Di Valentin, G. Pacchioni, A. Selloni, Chem. Mater. 17 (2005) 6656.
[42] N. Serpone, J. Phys. Chem. B 110 (2006) 24287.
[43] M. Addamo, V. Augugliaro, A. Di Paola, E. Garcia-Lopez, V. Loddo, G. Marci, R. Molinari, L. Palmisano, M. Schiavello, J. Phys. Chem. B 108 (2004) 3303.
[44] E.P. Barrett, L.G. Joyner, P.P. Halenda, J. Am. Chem. Soc. 73 (1951) 373.
[45] A. Weibel, R. Bouchet, F. Boulc', P. Knauth, Chem. Mater. 17 (2005) 2378.
[46] V. Nadtochenko, N. Denisov, A. Gorenberg, Y. Kozlov, P. Chubukov, J.A. Rengifo, C. Pulgarin, J. Kiwi, Appl. Catal. B 91 (2009) 460.
[47] S. Bae, S. Kim, S. Lee, W. Choi, Catal. Today 224 (2014) 21.
[48] S.Y. Chae, M.K. Park, S.K. Lee, T.Y. Kim, S.K. Kim, W.I. Lee, Chem. Mater. 15 (2003) 3326.
[49] W.A. Daoud, J.H. Xin, Chem. Commun. (2005) 2110.
[50] M.P. Finnegan, H. Zhang, J.F. Banfield, Chem. Mater. 20 (2008) 3443.
[51] Y. Ren, L.J. Hardwick, P.G. Bruce, Angew. Chem. Int. Ed. 49 (2010) 2570.
[52] D. Reyes-Coronado, G. Rodríguez-Gattorno, M.E. Espinosa-Pesqueira, C. Cab, R. de Coss, G. Oskam, Nanotechnology 19 (2008), 145605.
[53] J.I. Paredes, A. Martínez-Alonso, P.X. Hou, T. Kyotani, J.M.D. Tascón, Carbon 44 (2006) 2469.
[54] X. Sheng, B. Wouters, T. Breugelmans, A. Hubin, I.F.J. Vankelecom, P. P. Pescarmona, ChemElectroChem 1 (2014) 1198.
[55] K.S.W. Sing, D.H. Everett, R.A.W. Haul, L. Moscou, R.A. Pierotti, J. Rouquerol, T. Siemieniewska, Pure Appl. Chem. 57 (1985) 603.
[56] W. Lueangchaichaweng, L. Li, Q.Y. Wang, B.L. Su, C. Aprile, P.P. Pescarmona, Catal. Today 203 (2013) 66.
[57] G. Riegel, J.R. Bolton, J. Phys. Chem. 12 (1995) 4215.
[58] U. Diebold, Surf. Sci. Rep. 48 (2003) 53.
[59] D.O. Scanlon, C.W. Dunnill, J. Buckeridge, S.A. Shevlin, A.J. Logsdail, S. M. Woodley, C.R.A. Catlow, M.J. Powell, R.G. Palgrave, I.P. Parkin, G.W. Watson, T.W. Keal, P. Sherwood, A. Walsh, A.A. Sokol, Nat. Mater. 12 (2013) 798.
[60] M. Hirano, C. Nakahara, K. Ota, O. Tanaike, M. Inagaki, J. Solid State Chem. 170 (2003) 39.
[61] K. Okada, N. Yamamoto, Y. Kameshima, A. Yasumori, K.J.D. MacKenzie, J. Am. Ceram. Soc. 84 (2004) 1591.
[62] R. Castillo, B. Koch, P. Ruiz, B. Delmon, J. Mater. Chem. 4 (1994) 903.
[63] G. Zhang, F. Teng, Y. Wang, P. Zhang, C. Gong, L. Chen, C. Zhao, E. Xie, RSC Adv. 3 (2013) 24644.
[64] A.A. Umar, M. Yusri, A. Rahman, S.K. Saad, M.M. Salleh, Int. J. Electrochem. Sci. 7 (2012) 7855.
[65] S. Sakthivel, H. Kisch, Angew. Chem. Int. Ed. 42 (2003) 4908.
[66] X. Orignac, H.C. Vasconcelos, M.R. Almeida, J. Non-Cryst. Solids 217 (1997) 155.
[67] J.-Y. Ruzicka, F.A. Bakar, L. Thomsen, B.C. Cowie, C. McNicoll, T. Kemmitt, H.E. A. Brand, B. Ingham, G.G. Andersson, V.B. Golovko, RSC Adv. 4 (2014) 20649.
[68] R. Rodrigues, M. Gonçalves, D. Mandelli, P.P. Pescarmona, W.A. Carvalho, Catal. Sci. Technol. 4 (2014) 2293.
[69] C. Di Valentin, G. Pacchioni, A. Selloni, J. Phys. Chem. C 113 (2009) 20543.
[70] S. Sakthivel, M. Janczarek, H. Kisch, J. Phys. Chem. B 108 (2004) 19384.
[71] N. Daems, X. Sheng, I.F.J. Vankelecom, P.P. Pescarmona, J. Mater. Chem. A 2 (2014) 4085.
[72] Y. Nosaka, M. Matsushita, J. Nishino, A.Y. Nosaka, Sci. Technol. Adv. Mater. 2 (2005) 143.
[73] C. Di Valentin, G. Pacchioni, A. Selloni, S. Livraghi, E. Giamello, J. Phys. Chem. B 109 (2005) 11414.
[74] Y. Liu, H. Du, F.-S. Xiao, G. Zhu, W. Pang, Chem. Mater. 12 (2000) 665.
[75] P.C. Rowlette, C.A. Wolden, ACS Appl. Mater. Interfaces 1 (2009) 2586.
[76] N. Veronovski, P. Andreozzi, C. La Mesa, M. Sfiligoj-Smole, V. Ribitsch, Colloid Polym. Sci. 288 (2010) 387.
[77] Z. Wang, W. Cai, X. Hong, X. Zhao, F. Xu, C. Cai, Appl. Catal. B 57 (2005) 223.
[78] J. Zhang, Y. Wu, M. Xing, S.A.K. Leghari, S. Sajjad, Energy Environ. Sci. 3 (2010) 715.
[79] Although some visible-light-active TiO$_2$ photocatalysts have been reported to achieve the complete removal of probe compounds with shorter reaction times (few hours) compared to those reported here (see for example ref. 77), it should be underlined that the tests in the literature are typically performed with a much higher catalyst-to-probe ratio. In this work, we chose to tests our photocatalysts with low catalyst-to-probe ratio, and thus in demanding conditions under which it is not expected to achieve complete removal.
[80] G. Yang, Z. Jiang, H. Shi, T. Xiao, Z.J. Yan, Mater. Chem. 20 (2010) 5301.
[81] M. Chen, W. Chu, J. Hazard. Mater. 219-220 (2012) 183.